

Adversarial Prediction of Radiotherapy Treatment Machine Parameters*

Lyndon Hibbard

Elekta Inc., St. Charles MO 63303, USA

Lyn.Hibbard@elekta.com

<http://www.elekta.com/>

Abstract. Modern external-beam cancer radiotherapy applies prescribed radiation doses to tumor targets while minimally affecting nearby vulnerable organs-at-risk (OARs). Creating a clinical plan is difficult and time-consuming with no guarantee of optimality. Knowledge-based planning (KBP) mitigates this uncertainty by guiding planning with probabilistic models based on populations of prior clinical-quality plans. We have developed a KBP-inspired planning model that predicts plans as realizations of the treatment machine parameters. These are tuples of linear accelerator (Linac) gantry angles, multi-leaf collimator (MLC) apertures that shape the beam, and aperture-intensity weights that can be represented graphically in a coordinate frame isomorphic with projections (beam’s-eye views) of the patient’s target anatomy. These paired data train CycleGAN networks that estimate the MLC apertures and weights for a novel patient, thereby predicting a treatment plan. The dosimetric properties of the predicted plans agree with clinical plans to within a few percent, and take far less time to compute. The predicted plans can serve as lower bounds on plan quality, and as initializations for MLC aperture shape and weight refinement.

Keywords: Radiotherapy · Deep learning · Plan prediction.

1 Introduction

Cancer radiotherapy is based on two main premises. The first is that tumor cells are less competent to repair DNA strand breaks due to radiation than nearby normal cells. The second is that this biological difference is best exploited by irradiating the tumor with (possibly many) shaped beams of radiation performing a kind of forward tomography, matching the 3D target shape with a 3D dose. Planning a treatment personalized for each patient requires the physician to balance tumor dose with inevitable damage to nearby vulnerable OARs. Planning difficulty is increased by anatomy complexity and by a number of dose constraints to individual targets and OARs that may be greater than the number of structures. Maximizing plan quality by adjusting plan parameters is difficult as the effects of any change can be difficult to anticipate. Treatment planning

* Supported by Elekta, Inc.

programs (TPPs) provide accurate models for dose physics, but they do not provide assurance that any given plan is close to the best possible, or provide direction to produce a better plan.

To mitigate planning uncertainty, knowledge-based planning (KBP) models dose properties [1], [2], [3], [4] and dose distributions [5], [6], [7] by sampling from probabilistic models learned from populations of clinical plans. The predicted properties must be converted into Linac/MLC parameters to enable the TPP to compute a treatment plan.

Here we report a new KBP-inspired approach that learns to predict the Linac/MLC parameters directly, bypassing intermediate steps, to produce realizations of accurate plans.

2 Methods

2.1 Patient Data Preparation and Treatment Planning

This study used 178 prostate datasets, planned identically, each starting with planning CT images and anatomy contours, to obtain volume modulated arc therapy (VMAT) plans [8]. The cases were anonymized and the contours were curated to conform to the RTOG 0815 standard [9]. The anatomy structures included the prostate, bladder, rectum, femoral heads, anus, penile bulb, seminal vesicles and the patient external contour. The targets are a pair of nested planning target volumes (PTVs); PTV1 enclosed the prostate plus a margin and PTV2 enclosed PTV1 and the seminal vesicles plus an additional margin. We obtained optimal dose fluence maps using the Erasmus-iCycle program [10], [11] following the prostate objectives and constraints in [12]. The fluence maps were input to Elekta Monaco (v. 5.11) to obtain clinical, deliverable VMAT plans, or the ground truth (GT) plans. The 178 cases were divided into training (138), validation (20), and test (20) sets.

The VMAT treatment is specified by the apertures' shapes and their intensity weights at 100 or more discrete linac gantry angles. The MLC creates a 2D beam profile, normal to the beam direction, by opening gaps between opposing banks of tungsten leaves. The gantry angles, aperture leaf positions, and intensity weights are collectively the control points. During treatment the linac gantry revolves continuously around the patient and the instantaneous linac radiation output and MLC beam shapes at any real angle are interpolated from the flanking control points. In this way, the control points or machine parameters constitute the deliverable treatment plan.

2.2 Data Reformatting for Supervised Learning

The target anatomy and the VMAT control points have fundamentally different representations—anatomies are rectilinear arrays of intensities and control points are vectors of real MLC leaf positions, plus scalar aperture weights and gantry angles. These data domains are connected by matching graphical images of the

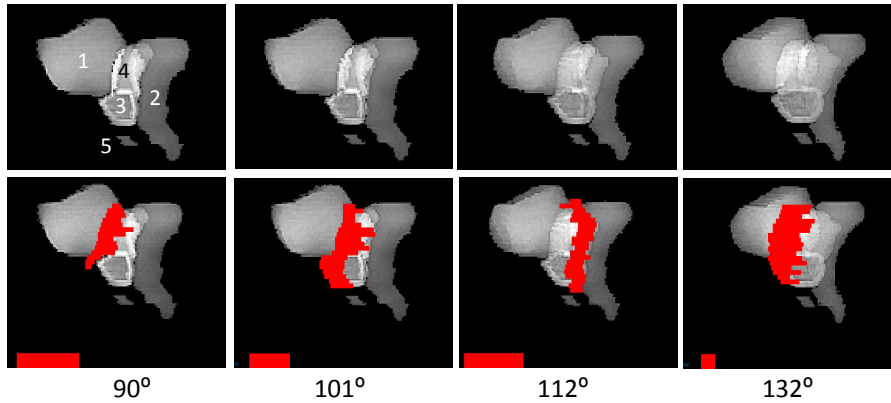


Fig. 1. Anatomy projections (top) and overlaid ground truth apertures (red, bottom) for a prostate target at four gantry angles. The challenge for radiotherapy is to irradiate the target volume (prostate (3) and seminal vesicles (4) plus margins) with the prescribed dose while sparing the adjacent organs-at-risk (OARs; bladder (1), rectum (2), and penile bulb (5)). The red bar length encodes the apertures' weights. The combined gantry angles, apertures and aperture weights are sufficient to specify a treatment plan. The apertures typically sweep back and forth across the target several times during one 2π arc to produce a clinical dose distribution. See text for more details.

MLC leaf apertures with beam's-eye-view projection images of the corresponding anatomy taken at the same gantry angle, and projected onto the normal plane containing the treatment isocenter (Fig. 1). The plan isocenter that is the point on the gantry axis of rotation that is also the perpendicular projection of the center of the MLC. The isocenter is also a reference point in the target volume providing a common origin for both the anatomy and treatment machine coordinate frames.

The CT images and the structure contours were transformed into OAR and PTV 3D binary masks, weighted, summed, and reformatted to a single 3D 8-bit image in the original CT frame. They were designed to emphasize the target volumes' edges from all directions. These 3D anatomy maps were resampled as projections using the forward projection function of the cone beam CT reconstruction program RTK [13]. Graphical images of the apertures were created from the MLC leaf positions and aligned with the plan isocenter and oriented and scaled to match the projections. The projection and aperture images were created at 128 equi-spaced gantry angles producing one projection and one aperture image at each angle. Each of these 2D images has dimensions 128x128 pixels (1.5 mm pixel spacing throughout) so the complete data for each patient consisted of two 128^3 volumes—one a stack of the projections and the second a stack of the aperture graphic images. An example of this data is shown in Fig. 1.

The graphical images also include a bar at the lower left whose length encodes the weight (cumulative meterset weight) or dose increment for that control point.

For 100 or more control points, the weights typically range in value from 0.001 to 0.01 and the space allotted for the bar length easily enables weight representation to within about 1% of a typical weight increment.

Finally, the ground truth plans set the collimator angle to 5° but for training the aperture graphic was depicted at 0° . After training, the test inferred apertures' leaf positions were re-written back into DICOM RT Plan files with collimator settings at 5° .

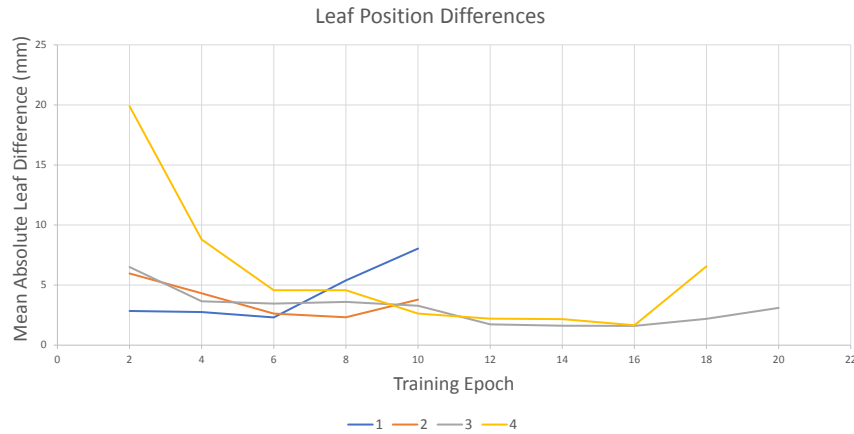


Fig. 2. Training histories for 3D CycleGAN networks learning MLC apertures and weights. Plotted here are the mean absolute MLC leaf position differences in millimeters (MALD) between GT and CycleGAN plans for the 20 test cases not used in training. The four histories correspond to four training regimes differing by learning rate schedule. A network model was saved at every 2 epochs to generate test plans and leaf position differences. All the training regimes produced minima at or below 2.3 mm. (See Table 1.)

2.3 Deep Learning Network and Training

Generative adversarial networks (GANs) have recently become essential technologies for data modeling and inference [14], [15]. Here we use a GAN to perform voxel-wise binary classification of aperture and weight-bar voxels. That is, is a voxel in an aperture or weight-bar or not? (Fig. 1.)

The results presented here were obtained with a CycleGAN network [16] but with paired data conditioned as for the pix2pix conditional GAN [17]. The full objective function is that used in [16] plus the identity loss. The discriminator network is a (70, 70, 70) PatchGAN with layer structure C18-C36-C76-C152-C304-C304 where C is a convolution/instance normalization[18]/LeakyReLU block with kernel (4, 4, 4) and stride (2, 2, 2), and k equals the number of filters

for each C_k . The last layer is a convolution to produce a 1D output with mean squared error loss. The generator is a 3D U-Net [19], [20] with six levels each for the encoding and decoding branches. The encoding branch layers are E18-E36-E54-E72-E90-E108 where each E_k contains two convolution/LeakyReLU/batch normalization [21] blocks with a densenet array of skip connections, kernel (3, 3, 3) and stride (1, 1, 1), and k equals the number of filters. The decoding branch is likewise D108-D90-D72-D54-D36-D18 where each block D_k contains a convolution transpose layer and two convolution/LeakyReLU/batch normalization blocks with kernel and stride dimensions and densenet skip connections like those of the encoding branch. The training batch size was a single 3D volume pair. The four CycleGAN losses were weighted as: adversarial (F), adversarial (G), cycle consistent, identity = 10:10:5:1. The numbers of filters used were the largest possible given the available gpu memory. The ADAM optimizer [22] was used throughout. The network was coded in Keras [23] with TensorFlow [24] and based partly on a Keras example CycleGAN code [25]. Four studies are presented here with the training conditions listed in Table 1.

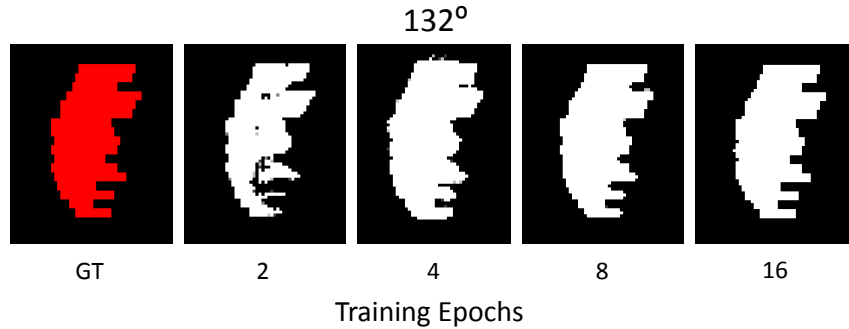


Fig. 3. Demonstration of the visual agreement of the inferred apertures with the corresponding GT aperture. This is the 132° aperture from Fig.1, from Study 4, Epoch 16 in Fig.2. The inferred leaf positions are extracted from left and right side boundaries of the white figures, and those at epoch 16 agree most closely with the ground truth aperture.

Table 1. Learning Rate (LR) Studies.

Study	Generator LR	Discriminator LR	LR Schedule	min-Epoch	MALD
1	10^{-3}	10^{-6}	LRs constant all epochs	6	2.31
2	10^{-4}	10^{-4}	LRs constant all epochs	8	2.32
3	10^{-4}	10^{-4}	LRs/4.0 at Epoch 5	14	1.62
4	10^{-3}	10^{-4}	LRs constant all epochs	16	1.65

The goal result is to input the inferred apertures and weights to a TPP to calculate the dose distribution and derived plan quality metrics. However, this is too expensive a calculation to be performed for all the possible epoch-interval models. Instead, we computed the mean absolute leaf position differences (MALD) between the CycleGAN and GT plans, over all control points for all 20 test cases, for each epoch-model. Fig. 2 plots the MALD values for four learning studies where models were saved at every two epochs. Each of these studies produced at least one model with a MALD of 2.3 mm or less. Table 1 lists the minimum-MALD epoch and MALD value for the four studies. Fig. 3 shows the gradual improvement of the 132° aperture from study 4 (Fig. 2) at the epochs indicated.

3 Results

3.1 Plan Quality Overview Via Dose Volume Histograms

The cumulative dose volume histogram (DVH) depicts the fraction of a structure’s voxels receiving dose greater than or equal to the dose on the horizontal axis. Fig. 4 displays the DVHs for all the targets and OARs for the Study 4, Epoch 16 model described in Figs. 2 and 3. The OAR DVHs occupy the lower left of the figure and the target DVH curves are at the upper right. The CycleGAN DVHs are the solid lines and the ground truth plan’s DVHs are the dashed lines. In Fig. 4 the CycleGAN and ground truth OARs are nearly coincident while the target DVHs show close agreement. This pattern of OAR and target DVH agreement was observed for all the low-MALD models.

3.2 Dosimetric Properties of the Inferred Treatment Plans

Fig. 5 presents another view of the Study 4, Epoch 16 inferred doses. Plotted are the mean absolute %-differences, $1/N \sum_{n=1}^N [100 * |CycleGAN_n - GT_n| / GT_n]$ for the $N=20$ test cases, for each of a set of dose metrics, for OARs bladder and rectum (top) and targets PTV1 and PTV2 (below). (Error bars represent $\pm 1\sigma$.) Dmean and Dmax are the mean and maximum doses observed for each structure and V65Gy(%) is the volume percent of a structure receiving a dose of 65 Gray (Gy). D98% is the largest dose seen by 98% of the lower-dose target voxels and D2% is the smallest dose seen by 2% of the highest-dose target voxels. For comparison, the prescribed dose for the ground truth plans is 78 Gy.

The OAR (upper) plots show most of the dose-comparison measures at or below 3%. The trends across the series show a declining difference between the V65Gy and the Dmax and Dmean metrics, and general decline in all the measures across the four learning studies. The targets’ plots (lower) present a similar picture with declining differences between Dmax and Dmean within models, and overall declines in all the measures from studies 1 to 4.

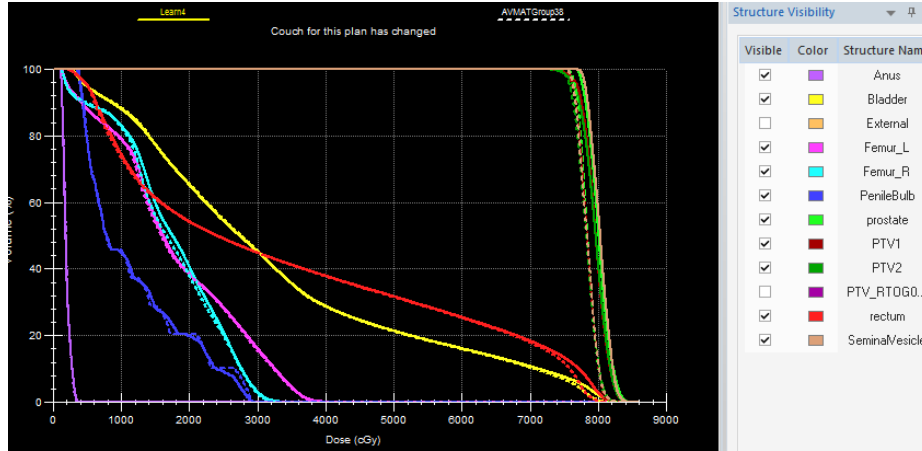


Fig. 4. Dose-volume histograms (DVHs) depict that fraction of a structure’s voxels receiving dose greater than or equal to the dose on the horizontal axis. Targets (PTV1, PTV2) cluster at upper right and OARs occupy the lower left portion of the figure. Two plans are compared here: a single patient’s CycleGAN (solid) plan from study 4, epoch16 (Fig.2), and the GT plan (dashed). All the OAR DVH-pairs are nearly co-incident and the target curves agree closely.

3.3 Predicted-Plan v. Predicted-Dose Results

Comparison with published work is problematic since these results and those of other investigators were obtained under different conditions. Nguyen et al. [7] presented a dose prediction study using a 2D U-Net on 88 prostate cases (training(80); test (8)). Models were learned using 10-fold cross-validation; the best performing model was used for testing. They found [7] Table 1, mean absolute Dmax and Dmean %-differences of 1.80, 1.09 (PTV), 1.94, 4.22 (bladder), and 1.26, 1.62 (rectum), respectively. The corresponding Dmax, Dmean absolute %-differences for the Study4, Epoch 16 model are: 2.45, 1.39 (PTV1), 2.26, 1.27 (PTV2), 1.76, 0.69 (bladder), and 1.80, 0.97 (rectum), respectively. At least we can say that these predicted-plan results are similar to the predicted-dose results of [7].

4 Summary and Discussion

This is the first report to our knowledge of a deep learning model for radiotherapy treatment plans realized as Linac/MLC parameters. The 3D CycleGAN network predicts the parameters for a novel-patient anatomy rendered as a 3D array of beam’s-eye-view projections, and the resulting apertures and their weights can be directly input into a TPP for dose calculation and treatment delivery if desired. In general, the 3D CycleGAN network tends to slightly under-estimate the PTV doses, but the OAR sparing is very close to that of the training data.

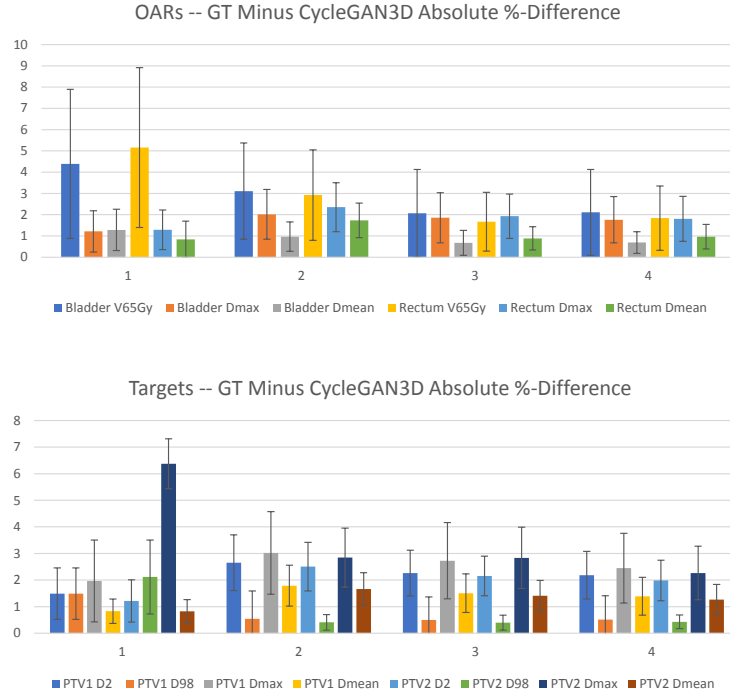


Fig. 5. Bar plots of mean absolute %-difference (GT - CycleGAN) dosimetric measures for OARs (upper) and targets (lower) for 20 test cases, for each of four learning studies. Error bars represent $\pm 1\sigma$. The OAR plots are for bladder and rectum only. V65Gy is the fraction of a structure receiving a dose greater than or equal to 65Gy, a large dose since the prescribed target dose is 78Gy. Dmax and Dmean are the maximum and mean doses for the structure. D98% is the maximum dose seen by target voxels receiving at least 98% of the lower doses and D2% is the minimum dose seen by 2% of the higher-dose voxels. Overall, the average absolute differences for both OARs and targets are mostly 3% of the GT value or less.

TPPs must provide a heuristic control point initialization to begin VMAT plan computation, and it would be interesting to know how the CycleGAN predicted control points compare to the heuristic control points. First, the TPP-supplied control points always have to be optimized with respect to treatment objectives requiring 30-60 min for a typical prostate planned using the criteria of this study. The CycleGAN predictions learned from a population of high quality plans are already close (on average) to the ground truth plans (see Figure 5) and because they are re-composed as DICOM RTPlan files, they could potentially be used for treatment. When refinement is required, the CycleGAN control point refinement typically takes less time than that of the default TPP initial control points (data not shown). Studies of this and other properties of the CycleGAN predicted plans are in progress.

The 3D CycleGAN models can serve several functions. The network inferences provide a lower bound to the plan quality achievable using the plan objectives and constraints for this particular radiotherapy treatment. Thus, if a new plan in progress is not as good as the network-predicted plan, the planner knows at least that a better plan is possible, knowledge not available with current technology. Second, these inferences may be input to a TPP (e.g., Elekta Monaco) for MLC aperture shape and weight refinement for a warm start dose calculation. Either way, a clinic without deep physics expertise or with very demanding treatment throughput requirements could achieve better efficiency and plan quality.

5 Acknowledgements

The author would like to thank Peter Voet, Hafid Akhiat, Spencer Marshall, and Michel Moreau for help creating the prostate plans and for many helpful discussions.

References

1. Kazhdan, M., Simari, P., McNutt, T.: *et al.*, A Shape Relationship Descriptor for Radiation Therapy Planning. *MICCAI 2009*, Part II, LNCS 5762, pp. 100–108 (2009)
2. Wu, B., Ricchetti, B., Sanguinetti, G.: *et al.*, Patient geometry-driven information retrieval for IMRT treatment plan quality control. *Medical Physics* **36**(12), 5497–5505 (2009)
3. Zhu, X., Ge, Y., Li, T., Thongphiew, D., Yin, F.-F., Wu, Q.J.: A planning quality evaluation tool for prostate adaptive IMRT based on machine learning. *Medical Physics* **38**(2), 719–726 (2011)
4. Appenzoller, L.M., Michalski, J.M., Thorstad, W.L., Mutic, S., Moore, K.L.: Predicting dose-volume histograms for organs-at-risk in IMRT planning. *Medical Physics* **39**(12), 7446–7461 (2012)
5. Shiraishi, S., Moore, K.L.: Knowledge-based prediction of three-dimensional dose distributions for external beam radiotherapy. *Medical Physics* **43**(1), 378–387 (2012)

6. McIntosh, C., Purdie, T.G.: Contextual Atlas Regression Forests: Multiple-Atlas-Based Automated Dose Prediction in Radiation Therapy. *IEEE Trans Medical Imaging* **35**(4):1000–1012 (2016)
7. Nguyen, D., Long, T., Jia, X.: A feasibility study for predicting optimal radiation therapy dose distributions of prostate cancer patients from patient anatomy using deep learning. *Sci Rep* **9**, 1076 (2019). <https://doi.org/10.1038/s41598-018-37741-x>.
8. Unkelbach, J., Bortfeld, T., Craft, D., Alber, M., Bangert, M., Bokrantz, R., Chen, D., Li, R., Xing, L., Men, C., Nill, S., Papp D., Romeijn, E., Salari, E.: Optimization approaches to volumetric modulated arc therapy planning, *Medical Physics*, **42**(3), 2015.
9. RTOG Homepage, <http://www.rtog.org/>. Last accessed 10 Mar 2020
10. Breedveld, S., Storchi, P.R.M., Heijmen, B.J.M.: The equivalence of multi-criteria methods for radiotherapy plan optimization. *Physics in Medicine and Biology* **54**, 7199–7209 (2009)
11. Breedveld, S., Storchi, P.M.R., Voet, P.W.J., Heijmen, B.J.M.: iCycle: Integrated, multicriterial beam angle, and profile optimization for generation of coplanar and noncoplanar IMRT plans. *Medical Physics* **39**(2), 951–963 (2012)
12. Wang, Y., Breedveld, S., Heijmen, B.J.M., Petit, S.F.: Evaluation of plan quality assurance models for prostate cancer patients based on fully automatically generated Pareto-optimal treatment plans. *Phys Med Biol.* **61**, 4268–4282 (2016)
13. Rit, S., Vila Oliva, M., Brousmiche, S., Labarbe, R., Sarrut, D., Sharp, G. C., The Reconstruction Toolkit (RTK), an open-source cone-beam CT reconstruction toolkit based on the Insight Toolkit (ITK), *Journal of Physics: Conference Series*, 489, 012079, 2013.
14. Goodfellow, I., Pouget-Abadie, J., Mirza, M. *et al.*: Generative Adversarial Nets. *arXiv:1406.2661v1*, 2014.
15. Goodfellow, I.: NIPS 2016 Tutorial: Generative Adversarial Networks. *arXiv:1701.00160v4* (2016)
16. Zhu, J.-T., Park, T., Isola, P., Efros, A.A.: Unpaired image-to-image translation using cycle-consistent adversarial networks, *arXiv:1703.10593v1* (2017)
17. Isola, P., Zhu, J.-T., Zhou, T., Efros, A.A.: Image-to-image translation with conditional adversarial networks, *arXiv:1611.07004v1* (2016)
18. Ulyanov, D., Vedaldi, A., Lempitsky, V.: Instance Normalization: The missing ingredient for fast stylization, *arXiv:1607.08022v3* (2017)
19. Ronneberger, O., Fischer, P., Brox, T.: U-Net: Convolutional Networks for Biomedical Image Segmentation. *arXiv.1505.04597v1* (2015)
20. Milletari, F., Navab, N., Ahmadi, S.-A.: V-Net: Fully Convolutional Neural Networks for Volumetric Medical Image Segmentation, Fourth International Conference on 3D Vision (3DV) (2016)
21. Ioffe, S., Szegedy, C.: Batch Normalization: Accelerating Deep Network Training by Reducing Internal Covariate Shift. *arXiv:1502.03167v3* (2015)
22. Kingma, D.P., Ba, J.L.: ADAM: A Method for Stochastic Optimization. *arXiv:1412.6980v8* (2015)
23. Chollet, F.: *Deep Learning with Python*, Manning, Shelter Island, New York (2018)
24. Abadi, M., Agarwal, A., Barham, P., *et al.*: TensorFlow: Large-Scale Machine Learning on Heterogeneous Distributed Systems. Google Research. <https://www.tensorflow.org/> (2015)
25. Brownlee, J.: *Generative Adversarial Networks with Python*, <http://machinelearningmastery.com>, 2019.